



A simple route for preparation of textured WO₃ thin films from colloidal W nanoparticles and their photoelectrochemical water splitting properties



S. Emin^{a,*}, M. de Respinis^b, M. Fanetti^a, W. Smith^b, M. Valant^a, B. Dam^b

^a Materials Research Laboratory, University of Nova Gorica, SI-5000, Slovenia

^b Materials for Energy Conversion and Storage (MECS), Department of Chemical Engineering, Delft University of Technology, 2600 GA Delft, The Netherlands

ARTICLE INFO

Article history:

Received 18 August 2014

Received in revised form

21 November 2014

Accepted 24 November 2014

Available online 30 November 2014

Keywords:

Photoelectrochemical water splitting

Colloidal nanoparticle

Tungsten trioxide

ABSTRACT

Colloidal tungsten (W) nanoparticles (NPs) were synthesized by pyrolysis of W(CO)₆ precursor in a mixture of 1-octadecene, oleylamine and oleic acid at ~230 °C under Ar atmosphere. The metallic W NPs were spin-coated on fluorine-doped tin oxide (FTO) substrates and later were transformed to WO₃ phase by heat treatment at 500 and 550 °C. We prepared WO₃ thin films with different thicknesses which we used in photoelectrochemical water splitting. The highest achieved photocurrent was ~830 μA/cm² at 1.9 V vs. reference reversible hydrogen electrode (RHE) with the 900 nm thick WO₃ film. Incident photon-to-current conversion efficiency (IPCE) showed that the quantum efficiency of WO₃ thin films can reach up to 66% at 320 nm. Characterization of W NPs and WO₃ thin films was carried out with UV–vis absorption spectroscopy, diffused reflectance spectroscopy, X-ray diffraction, transmission electron microscope and scanning electron microscope. The procedure given herein is a novel fabrication approach for the preparation of textured WO₃ thin films where metallic W NPs are used as a precursor material. The proposed method can be generalized and extended to the preparation of other types of textured metal oxide thin films.

© 2014 Elsevier B.V. All rights reserved.

1. Introduction

In the last decade, there has been intensive research on photoelectrochemical (PEC) water splitting due to its potential for economical production of solar fuels [1,2]. Different kind of semiconductor materials have been synthesized and studied for this purpose. Photoanodes based on n-type metal oxides such as TiO₂ [3,4], α-Fe₂O₃ [5,6] and WO₃ [7–9] have been investigated due to their environmental friendliness, low cost, earth abundance and chemical stability. Unlike TiO₂, which does not absorb visible (Vis) light due to its large band-gap (E_g) exceeding 3.2 eV, semiconductor WO₃ is preferred in the PEC water splitting studies because it has narrower band-gap in the order of 2.5–2.8 eV [8]. Calculations showed that the narrower E_g values of WO₃ can result in ~6% solar-to-hydrogen (STH) conversion efficiency when used in a single-junction PEC cell [10]. Another advantage of WO₃ is due to its intrinsic carrier transport properties such as the moderate hole diffusion length (L_h) which is in the order of ~150 nm.

This compares favorably with 10 nm for TiO₂ (rutile single crystal, [11]) and ~3 nm for α-Fe₂O₃ [12]. The longer L_h in WO₃ can result in lower electron–hole recombination rate. Introducing textures in semiconductors like one-dimensional (1D, nanorod, etc.), two-dimensional (2D, planar film, plate, etc.) or three-dimensional (3D, porous film) structures which have dimensions comparable or shorter than L_h is a common strategy to reduce recombination. For example, because of this reason 1D WO₃ nanoflakes have been found to be more efficient in water splitting than their bulk counterpart [13,14]. Moreover, hierarchical structures are useful not only because of the fact that they could provide a short diffusion path for the photogenerated carriers, but they also exhibit high surface area, beneficial to accelerate chemical reactions or show enhanced light absorption due to light trapping effect [15].

In recent years, various techniques have been developed for preparation of textured WO₃ thin films for use in the PEC water splitting. Some of these techniques include chemical vapor deposition (CVD) [16], glancing angle deposition [17], electrodeposition [18], sol–gel precipitation [19] or hydrothermal synthesis [20]. Sometimes the fabrication of an electrode can also include combinations of methods like in the case of wet-chemistry methods where nanoparticles (NPs) are first synthesized in solutions and

* Corresponding author. Tel.: +386 53653538.

E-mail address: saim.emin@ung.si (S. Emin).

later deposited onto solid substrates by spin-coating or doctor blading to form a textured semiconductor electrode [21]. Plasma processing of metallic films is another example of advanced method for preparation of the textured metal oxide thin films. In a recent study, de Respinis et al. [22] have used a plasma technique combined with a two-step oxidation to fabricate textured WO_3 thin films onto metallic tungsten substrates for PEC water splitting studies. This fabrication approach looks promising due to the potential applicability to other metals, however the expensive plasma processing setup may limit its widespread application. For scalability reasons, the wet-chemistry synthesis approach seems more promising. The following advantages can be foreseen for the wet-chemistry methods: (i) the synthesis of NPs involves moderate temperatures, (ii) the experimental setup is not expensive and (iii) the final (nano)material is prepared in the form of powder, stock solution or paste which can be easily spin-coated onto solid substrates.

Here we report a facile route for the preparation of textured WO_3 thin films by using colloidal W NPs. The colloidal W NPs were synthesized following a similar approach to the so-called hot-matrix synthesis used for the preparation of semiconductor nanocrystals (also known as quantum dots, QDs) [23]. The synthetic method involves pyrolysis of organometallic compounds in high boiling point organic solvent such as 1-octadecene (1-ODE) which upon dissociation gives metallic NPs. Recently, this approach was used for pyrolysis of $\text{M}(\text{CO})_6$ ($\text{M} = \text{Cr}, \text{Mo}, \text{W}$) in ionic liquids to produce metallic Cr, Mo and W NPs [24]. In a recent study, Vollmer et al. [25] showed that the decomposition of $\text{M}(\text{CO})_6$ in ionic liquids can be achieved easily by using microwave irradiation. They showed that microwave irradiation can cause the ionic solvent to heat up to 250°C which is high enough to decompose the $\text{M}(\text{CO})_6$ precursor and produce metallic NPs. In 2014, Schöttle et al. [26] extended the pyrolysis approach to metal chlorides such as WCl_6 to synthesize metallic W NPs. They conducted the synthesis of W NPs in liquid ammonia-based medium via reduction of WCl_6 with dissolved sodium. Although the latter synthesis presents an interesting approach, the use of the volatile ammonia and explosive/flammable sodium can be considered as a drawback. In this study, we carried out pyrolysis of $\text{W}(\text{CO})_6$ at 230°C in non-polar solvent 1-ODE containing a mixture of surfactants. Further, after coating the W NPs onto F-doped SnO_2 (FTO) substrates, we oxidized the obtained metallic W films to produce textured WO_3 films. As a final objective, we applied the obtained textured WO_3 thin films in photoelectrochemical (PEC) water splitting studies. To optimize the photogenerated current, which is a measure of the water splitting efficiency, we explored the effect of the oxidation temperature of the W films and WO_3 film thickness and on the photogenerated current as a photoanode for solar water splitting. The highest photocurrent of $\sim 830 \text{ mA/cm}^2$ at 1.9 V vs. RHE was obtained with a 900 nm thick WO_3 film. Incident photon-to-current efficiency (IPCE) studies showed that WO_3 electrodes exhibit IPCE values as high as 66%. The proposed approach herein for fabrication of textured WO_3 can be extended for the preparation of other metal oxide thin films.

2. Experimental

2.1. Materials

Hexacarbonyltungsten (97%, $\text{W}(\text{CO})_6$), oleic acid (99%, OA), oleylamine (70%, OLA), 1-octadecene (90%, ODE), chloroform (99.5%, CHCl_3) and ethanol (98%, EtOH) were purchased from Alfa Aesar.

2.2. Synthesis of W nanoparticles

The synthesis of W NPs was carried out under Ar atmosphere at $\sim 230^\circ\text{C}$. 1.44 g (4.0 mmol) $\text{W}(\text{CO})_6$, 0.22 g (2.0 mmol) OA, 1.06 (4.0 mmol) OLA and 25 ml ODE were added in a preheated (130°C) three-neck flask. The flask was kept at this temperature until $\text{W}(\text{CO})_6$ dissolved. Later, the reaction mixture was gradually heated to 230°C in 10 min and kept at that temperature for 1 h. The formation of W NPs was evidenced from the color change from transparent to dark. Once the reaction was completed, the flask was left to cool to 80°C . A mixture of EtOH: CHCl_3 (30:5 ml) was added to the obtained W NPs suspension. Then the suspension was centrifuged at 7000 rpm for 15 min. After decantation 5 ml of CHCl_3 was added in the centrifuge tube to dissolve W NPs. The final precipitation was done with 30 ml EtOH. The W NPs suspension was centrifuged. After drying at 40°C , we obtained 0.32 g of W NPs.

2.3. Fabrication of WO_3 electrodes

Fabrication of the textured WO_3 thin-film electrodes was achieved by spin-coating of W NPs onto the FTO substrates and subsequent calcination of the obtained metallic films at $\geq 500^\circ\text{C}$ for 60 min. The suspension of W NPs was prepared by dispersing the obtained W NPs in different volumes of CHCl_3 . For example, to produce 200 nm thick W film, we dissolved 0.32 g W NPs in 2 ml of CHCl_3 and spin-coated it at 1000 rpm for 20 s.

2.4. Characterizations

The crystal structure of the samples was determined using a Bruker D8 Advance X-ray diffractometer equipped with Cu X-ray source and LynXEye linear detector. Reflectance measurements were performed with DH-2000-BAL UV-VIS lightsource (Ocean Optics) and 2000 Pro CCD spectrometer (Maya). Absorbance spectra were recorded on a Lambda 35 UV-vis spectrophotometer (PerkinElmer). The morphology of the structures was studied with a JSM 7100F scanning electron microscope (SEM, JEOL) equipped with field-emission electron gun and coupled to an energy dispersive X-ray (EDS) spectrometer (Oxford Instruments). Transmission electron microscopy (TEM) studies were carried out with JEOL 2100F. PEC measurements were done in the three-electrode configuration in an aqueous 0.1 M Na_2SO_4 electrolyte solution (pH 6.4) electrolyte, where the electrode area was 0.283 cm^2 . An O-ring was placed between the thin film and the sample holder to allow an easy measurement of the area of the electrode in contact with the electrolyte and illuminated. The potential of the working electrode was controlled by a potentiostat (EG&G PAR283). A coiled Pt wire and an Ag/AgCl electrode (XR300, Radiometer Analytical) were used as the counter and reference electrodes, respectively. Voltammetry measurements were performed under simulated AM1.5 illumination (100 mW/cm^2) with a Newport Sol3A Class AAA solar simulator (type 94023A-SR3) with a scan rate of 10 mV/s. During the PEC measurements, the samples were illuminated with light from the front (electrolyte/ WO_3 /FTO) and back sides (FTO/ WO_3 /electrolyte). The potential values of I - V data were converted from Ag/AgCl to the reversible hydrogen electrode (RHE) scale according to the following equation: $E_{\text{RHE}} = E_{\text{Ag/AgCl}} + E^0_{\text{Ag/AgCl}} + (0.059 \times \text{pH})$ where E_{RHE} is the calculated potential versus RHE, $E_{\text{Ag/AgCl}}$ is the measured potential vs Ag/AgCl and $E^0_{\text{Ag/AgCl}} = 0.197 \text{ V}$ at 25°C [27]. Monochromatic photocurrents were measured with a 300 W Xenon arc lamp (Oriel, Model 6259) coupled to a grating monochromator (ActonSpectraPro 150i). An electronic shutter (Uniblitz LS6) was used and a long-pass colored glass filter (Schott, 3 mm thick) was placed between the monochromator and the sample to remove second-order diffracted light. The shutter was actuated with a frequency of 0.1 Hz, and the photocurrent was taken as the difference between

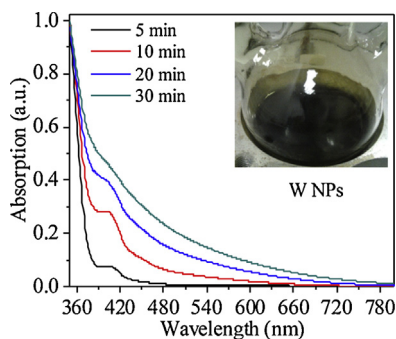


Fig. 1. UV–vis absorption spectra of W NPs in CHCl_3 taken at different reaction times. Inset is a flask containing W NPs obtained after 30 min synthesis.

the current when the shutter is opened and closed (3-s integration time and ~ 1.5 nm step size). The incident photon-to-current efficiency (IPCE) is calculated based on the formula [28]:

$$\text{IPCE (\%)} = \frac{1240 \times J \text{ (mA/cm}^2\text{)}}{P_{\text{light}} \text{ (mW/cm}^2\text{)} \times \lambda \text{ (nm)}} \times 100 \quad (1)$$

where J is the steady-state photocurrent density at a specific wavelength and λ is the wavelength of the incident light. P_{light} is the light intensity for wavelength λ at the film surface. The illumination intensity from the Xenon source was measured with a calibrated photodiode (Ophir PD300-UV).

3. Results and discussion

3.1. Synthesis of W NPs and their structural transformation to WO_3

Fig. 1 shows the absorption spectra of W NPs taken at different reaction times. The absorption peak at 390 nm can be assigned to

W plasmonic resonance. In the first 5 min, there is no significant absorption from the W NPs in the visible range. However, at longer reaction times, the absorption becomes broader and extends in the visible range. Furthermore, the absorption peak at 390 nm becomes less obvious after 20 min. The observed change in the absorption peak might be due to an increase in the mean size and the size polydispersity of the NPs. It is well known that metallic NPs show broader absorption peak with the increase in the size polydispersity [29].

Fig. 2a and b shows the TEM images of the obtained W NPs after 60 min reaction. The W NPs are very small and have a spherical shape. The average diameter (d) of these NPs is in the order of ~ 1.5 nm. The lack of lattice fringes in the TEM image evidences that the W NPs are amorphous. This finding is not a surprise for a synthesis carried out at $\sim 230^\circ\text{C}$ because crystallization of amorphous W NPs often require heat treatment at higher temperature $\sim 600^\circ\text{C}$ (in inert atmosphere). Similarly, Schöttle et al. [26] also reported formation of amorphous W NPs using a low-temperature technique in ammonia solution. The synthesis of crystalline W NPs at moderate temperature (e.g. 200°C) has only been reported for the techniques involving an ionic-liquid medium [24].

To produce WO_3 NPs, we oxidized the as-prepared W thin film at two different temperatures namely 500 and 550°C in air. Fig. 2c and d shows the TEM images of WO_3 NPs obtained after the oxidation step. Compared with W NPs, the obtained WO_3 NPs are a larger with a typical dimension in the order of 20–40 nm. The obtained final WO_3 NPs are crystalline as shown in the high-resolution (HR) TEM image. Fig. 2d shows a WO_3 crystallite with lattice fringes in the order of 0.37 nm which is attributed to the (110) interplanar spacing of monoclinic WO_3 .

Fig. 3 shows the XRD pattern of the W and WO_3 films deposited onto an FTO-coated glass alongside with the reference JPCDS data for SnO_2 and WO_3 . In the pattern of W-coated FTO (F:SnO_2) substrate, the peaks denoted as 110, 011 and 121 belong to SnO_2 phase (JCPDS 98-006-3198) [30]. The lack of diffraction from the W NPs

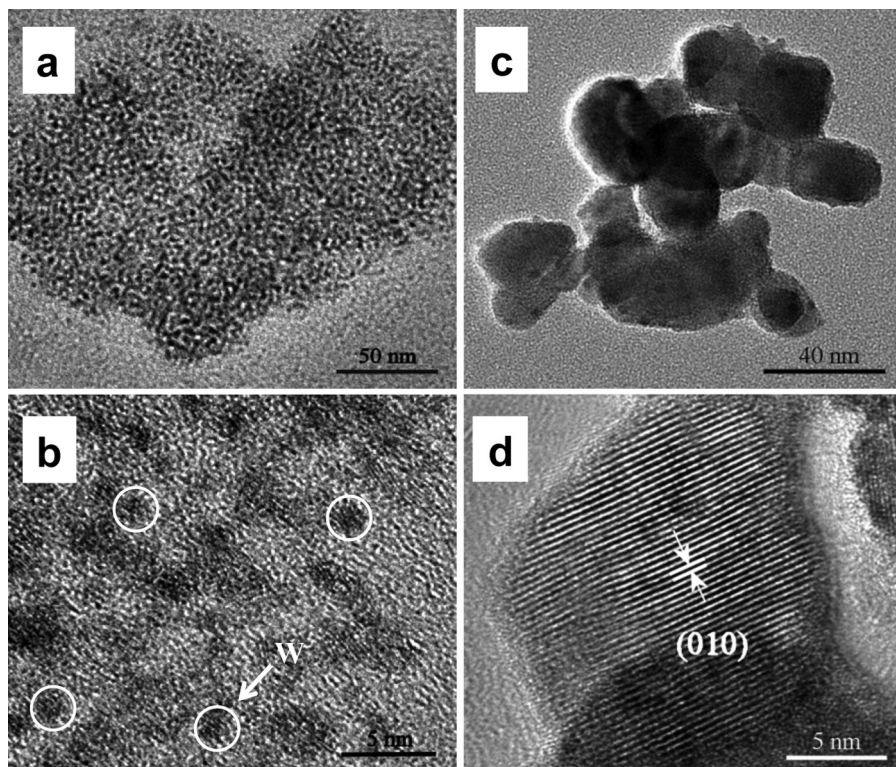


Fig. 2. TEM images of (a, b) W NPs at different magnifications. (c) TEM and (d) HR-TEM of WO_3 NPs. In (d) is shown the lattice fringes of (010) plane.

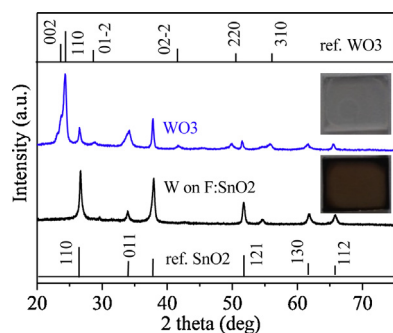


Fig. 3. XRD spectra of W and WO₃ thin films (~900 nm thick/550 °C) on FTO substrates. Inset are the photographs of W (brown) and WO₃ (white) samples.

agrees with the HR-TEM observations and confirms that the W NPs are amorphous. The sample denoted as WO₃ is obtained after oxidation of the W film at 550 °C. The XRD pattern of this sample matches with monoclinic WO₃ (JCPDS 98-003-9178) [31]. The intensive broad diffraction peak at ~24° is attributed to the two crystallographic planes of monoclinic WO₃ denoted as (002) and (110). In addition to the WO₃ peaks, we can also see diffraction peaks from the FTO substrate.

The optical properties of 200 nm thick WO₃ films prepared after oxidation at 500 and 550 °C are given in Fig. 4. The absorption coefficient, α , of the films was calculated using a simplified formula: $\alpha = d^{-1} \ln(T^{-1})$, where d is the film thickness and T is the transmittance [32]. The inset shows a Tauc plot from where the optical band gaps (E_g) were determined near the absorption onset assuming indirect transition [33–35]. The obtained E_g values of 2.53 eV for WO₃/550 °C and 2.55 eV for WO₃/500 °C are in agreement with the reported values for monoclinic WO₃, ~2.6 eV [36].

Fig. 5 shows the SEM images of the textured WO₃ thin films deposited on FTO substrates. Top-view images at different

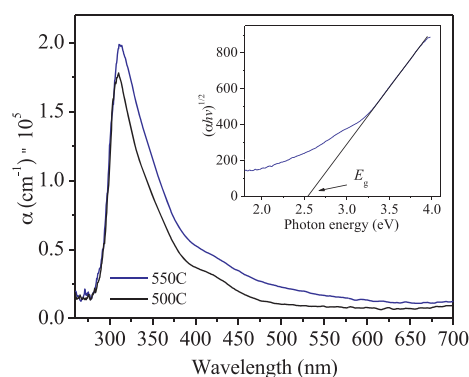


Fig. 4. Absorption coefficients (α) of WO₃ thin films obtained after calcination at 500 (black) and 550 °C (blue). The inset is a Tauc plot of the WO₃ film calcined at 500 °C from where is determined the optical band gap.

magnification are presented in Fig. 5a and b. The textured WO₃ thin films show a relatively smooth surface without any aggregates (on μm scale). At higher magnification, we observe small pores in the WO₃ film ranging from 20 to 100 nm in diameter. The pores are located deep enough in the film and most probably form channels through the entire WO₃ film. Fig. 5c and d shows cross-section images of the 200 and 900 nm thick WO₃ films. There is no significant difference in the WO₃ film morphology when the calcination was performed at 500 or 550 °C. In addition to SEM observations, we also performed EDS analysis of the 900 nm thick WO₃ film (see supporting info).

3.2. Photoelectrochemical studies of WO₃ electrodes

Fig. 6 shows the operational principles of the PEC cell that is used in the studies. A typical PEC cell is composed of FTO/WO₃ electrode

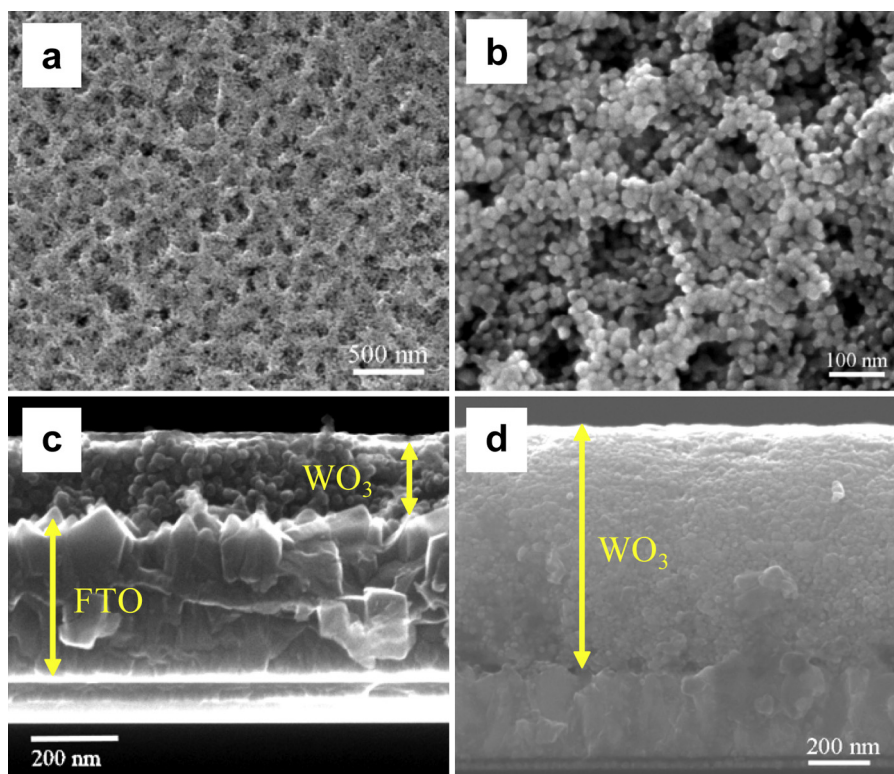


Fig. 5. (a, b) SEM images of WO₃ thin films obtained after calcination at 550 °C for 60 min (in air). The images are taken at different magnifications and viewed from the top. SEM cross-section images of (c) 200 nm and (d) 900 nm thick WO₃ films.

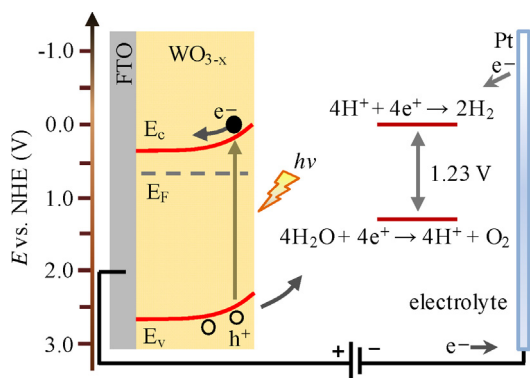


Fig. 6. Illustrative scheme showing the energy diagram of the WO_3 PEC cell under applied bias. The band diagram values were taken from ref. [20]. In the energy diagram, the Pt wire collects the electrons at E_F .

that is used as anode and Pt used as a cathode (counter) electrode. It is well known that WO_3 is an n -type semiconductor and when it is immersed in an electrolyte it will result in upward bending of the conduction and valence bands [8]. Upon illumination of the WO_3 film, the electrons (e^-) from the valence band (E_V) will be excited to the conduction band (E_C) leaving behind empty holes (h^+). These photoexcited electrons later can transfer to the FTO substrate. By using an external wire, the photoexcited electrons can be taken to the Pt electrode where they can be used to reduce H^+ to H_2 . Since the Fermi level (E_F) of WO_3 is below the H^+/H_2 energy level, an external bias is needed to elevate the E_F of Pt above the H^+/H_2 level, thus making the process possible [9]. As a result of these charge separations, the photoexcited electrons will participate in the H_2 evolution while the holes in the O_2 evolution.

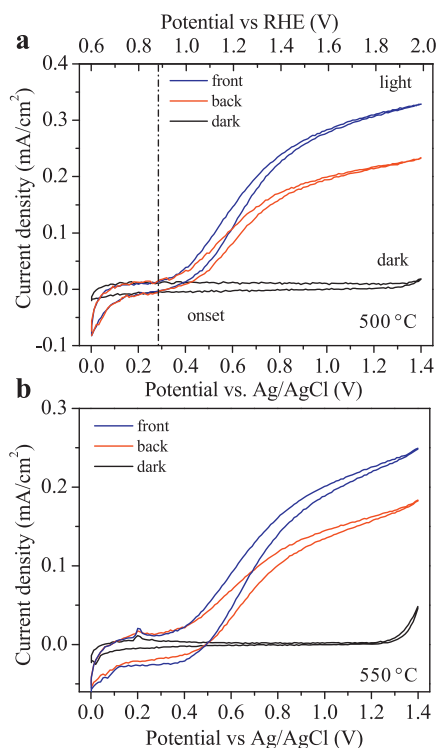


Fig. 7. I - V characteristics of 200 nm thick textured WO_3 thin films recorded in 0.1 M Na_2SO_4 (pH 6.4) with a scan speed of 50 mV/s. The measurements are performed in dark and under illumination ($100 \text{ mW}/\text{cm}^2$) from the front and back sides. The WO_3 films are obtained after calcination of W film at (a) 500°C and (b) 550°C for 60 min in air.

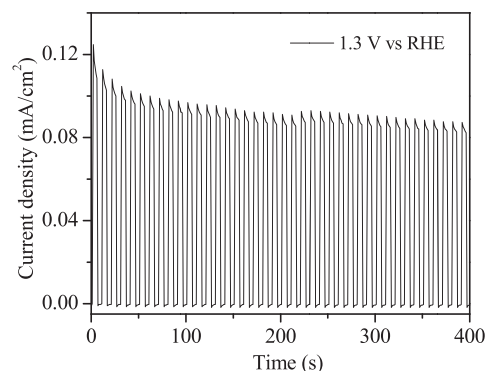


Fig. 8. Current density-time profile of 200 nm thick WO_3 films (calcined at 550°C) in 0.1 M Na_2SO_4 under applied bias of 1.3 V vs RHE. The photocurrent performance is recorded in frontside illumination under chopped light illumination.

Fig. 7 shows the current-voltage (I - V) characteristics of 200 nm thick textured WO_3 thin films obtained after calcination at 500 and 550°C . The I - V characteristics of these WO_3 films were compared both in the dark and under simulated solar illumination (1 sun, $100 \text{ mW}/\text{cm}^2$). While the dark current does not deviate from zero in the potential range from 0.6 to 1.9 V vs. RHE, the current recorded under illumination shows steep increase above 0.88 V vs. RHE (the onset potential). The observed increase in photocurrent density above the onset potential under illumination is usually assigned to water oxidation reaction ($2\text{H}_2\text{O} \rightarrow 2\text{O}_2 + 2\text{H}^+ + 4e^-$ at 1.23 V vs. RHE) that happens at the WO_3 electrode surface. Indeed, formation of small bubbles have been observed at the electrode surface upon illumination for about ~ 5 min (after several I - V scans) which are expected to be O_2 bubbles. Further, we tested the I - V response of WO_3 electrodes when they were illuminated from the front and the back sides. Here, the front side illumination is when light crosses the electrolyte/ WO_3 /FTO interfaces in this order. The photocurrent obtained from the 200 nm thick WO_3 films (calcined at 500°C) is higher under frontside than back-side illumination. This scenario also holds for the WO_3 film obtained after calcination at 550°C . Furthermore, the photocurrent of WO_3 sample oxidized at 500°C is $\sim 320 \mu\text{A}/\text{cm}^2$ (at 1.9 V vs RHE) and is much higher than for the sample oxidized at 550°C , which is $\sim 240 \mu\text{A}/\text{cm}^2$ at the same potential. The recorded I - V characteristics of all films are reproducible and for each series we tested two samples. Moreover, in the I - V characteristics of WO_3 films, there is a hysteresis between the forward and backward potential scans. The hysteresis observed in the potential range from 1.0 to 1.5 V vs. RHE could be associated to charge accumulation at the WO_3 /electrolyte interface due to some capacitive properties of this semiconductor material [37]. This hysteresis is largest for the sample calcined at 550°C . The observed photoelectrochemical behavior of WO_3 herein is consistent with WO_3 films reported by other groups [38].

Fig. 8 shows the current density vs. time (I - t) characteristics of WO_3 film in 0.1 M Na_2SO_4 under chopped illumination. The obtained I - t characteristics show the stability of WO_3 film for water splitting. During the first 50 s, the photocurrent density drops by 25% but with further illumination it stabilizes.

Fig. 9 shows the I - V characteristics of 450 and 900 nm thick WO_3 films. The highest photocurrent, which is about $830 \mu\text{A}/\text{cm}^2$ at 1.9 V (vs RHE), is achieved with the 900 nm thick WO_3 film in back illumination. This photocurrent value is almost three times higher than the one obtained with the 200 nm thick film. In the thicker films, the collection of photogenerated carriers in back configuration is more efficient than in front and the limiting factor which contributes to the observed photocurrent seems is the electrons collection efficiency (see **Fig. 9b**, inset). We propose that the thicker textured WO_3 film exhibits a higher surface area which in

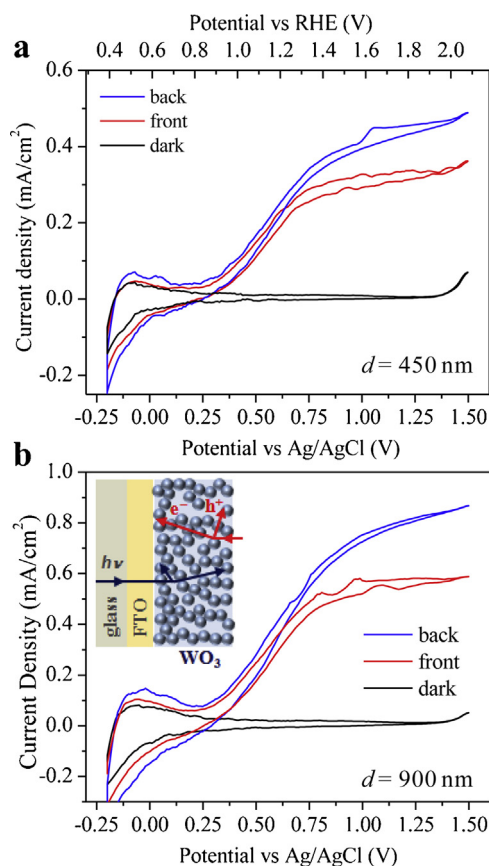


Fig. 9. *I*–*V* characteristics of textured WO_3 thin films in 0.1 M Na_2SO_4 (pH 6.4) recorded with a scan speed of 50 mV/s. The thicknesses of the WO_3 films obtained after calcination at 550 °C for 60 min (in air) are: (a) 450 nm and (b) 900 nm. Inset is a scheme showing the diffusion length for the photogenerated electrons and holes in WO_3 film after illumination from the front and back sides.

turn produces higher photocurrent (see IPCE and supporting info). A steep increase in cathodic current in the potential range from 0.8 to 0.4 V vs. RHE can be attributed to the following reduction reaction: $\text{WO}_3 + y\text{e}^- + y\text{H}^+ \rightarrow \text{H}_y\text{WO}_3$ [39]. Insertion of H^+ in the lattice of WO_3 changes the oxidation state of tungsten from W^{6+} to W^{5+} and due to this we observe increase in current. Fig. 10 gives the relation between photocurrent density and WO_3 film thicknesses. The highest photocurrent is achieved in the thicker films in front configuration.

To prove that the quantum efficiency is higher in the thicker films, we also performed IPCE studies. Fig. 11 shows the IPCE spectra of the 200 and 450 nm thick WO_3 films that are oxidized at

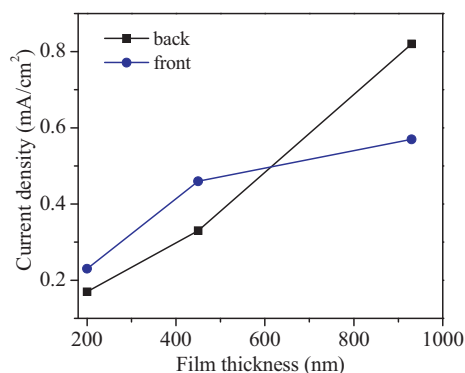


Fig. 10. Relation between photocurrent density vs. film thickness for the WO_3 samples calcined at 550 °C/1 h (in air).

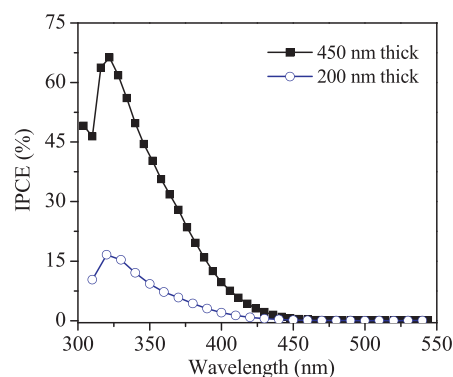


Fig. 11. IPCE spectra of 200 and 450 nm thick WO_3 thin films recorded in back illumination under applied bias of 1.3 V vs RHE. The films are calcined at 550 °C for 60 min in air.

550 °C. The IPCE peak at 320 nm is about ~66% for the 450 nm film and is only 17% in the 200 nm thick film. From this observation, it is clear that the lower quantum efficiency limits the performance of the 200 nm film. We expect that further improvement of WO_3 films properties can be achieved by controlling the morphology of WO_3 NPs inside the textured WO_3 film [18], by conducting the calcination of W films in O_2 -rich atmosphere [22], by addition of catalyst [40] or by doping the WO_3 films with various anions [41,42] or cations [43].

4. Conclusions

We have synthesized amorphous W NPs by conducting pyrolysis of $\text{W}(\text{CO})_6$ in 1-ODE solvent. The obtained W NPs were used as precursor material for preparation of the textured WO_3 thin films. The oxidation of W into WO_3 was carried out at 500 and 550 °C. The formation of WO_3 phase is associated with generation of (meso)pores in the film. The obtained textured WO_3 thin films were applied in PEC water splitting studies. We evaluated the effect of oxidation temperature on the PEC water splitting performance of WO_3 electrodes. We found that lower oxidation temperature (e.g. 500 °C) produces WO_3 films with better efficiency. The 200 nm thick WO_3 film oxidized at 500 °C shows 1.4 times (at 1.9 V vs RHE) higher photocurrent than the WO_3 film calcined at 550 °C. The obtained photocurrents values were higher in front illumination for both samples. Furthermore, we also tested the *I*–*V* characteristics of 450 and 900 nm thick WO_3 films. The highest recorded current density in the order of ~830 $\mu\text{A}/\text{cm}^2$ was achieved with the 900 nm thick WO_3 film in back illumination. Compared with the 200 nm thick WO_3 films the thicker films showed higher photocurrent in back illumination. The proposed approach which include oxidation of presynthesized metallic NPs can be applied also for the preparation of other metal oxide thin films for use in PEC water splitting studies.

Acknowledgements

This work was supported by European Commission under grant FP7 Marie Curie Career Integration Grant (HETMAT, Project No. 322114). The research is also financed in part by Slovenian Research Agency Programs No. P2-0377, Creative Core Project No. JR KJ - 430-44/2012/106 and the BioSolar Cells open innovation consortium, supported by the Dutch Ministry of Economic Affairs, Agriculture and Innovation.

Appendix A. Supplementary data

Supplementary material related to this article can be found, in the online version, at <http://dx.doi.org/10.1016/j.apcatb.2014.11.053>.

References

- [1] M.S. Prevot, K. Sivula, *J. Phys. Chem. C* 117 (2013) 17879–17893.
- [2] F.E. Osterloh, *Chem. Soc. Rev.* 42 (2013) 2294–2320.
- [3] Y. Wang, Y.-Y. Zhang, J. Tang, H. Wu, M. Xu, Z. Peng, X.-G. Gong, G. Zheng, *ACS Nano* 7 (2013) 9375–9383.
- [4] G. Wang, H. Wang, Y. Ling, Y. Tang, X. Yang, R.C. Fitzmorris, C. Wang, J.Z. Zhang, Y. Li, *Nano Lett.* 11 (2011) 3026–3033.
- [5] O. Zandi, J.A. Beardslee, T. Hamann, *J. Phys. Chem. C* 118 (2014) 16494–16503.
- [6] K. Sivula, F. Formal, M. Gratzel, *Chem. Sus. Chem.* 4 (2011) 432–449.
- [7] W. Smith, A. Wolcott, R.C. Fitzmorris, J.Z. Zhang, Y. Zhao, *J. Mater. Chem.* 21 (2011) 10792–10800.
- [8] D. Chandra, K. Saito, T. Yui, M. Yagi, *Angew. Chem. Int. Ed.* 52 (2013) 12606–12609.
- [9] Q. Chen, J. Li, X. Li, K. Huang, B. Zhou, W. Shanguan, *Chem. Sus. Chem.* 6 (2013) 1276–1281.
- [10] E.L. Miller, in: L. Vayssieres (Ed.), *On Solar Hydrogen and Nanotechnology*, John Wiley & Sons Pte Ltd, Singapore, 2009, pp. 3–35.
- [11] S. Hoang, S. Guo, N.T. Hahn, A.J. Bard, C.B. Mullins, *Nano Lett.* 12 (2012) 26–32.
- [12] L. Li, Y. Yu, F. Meng, Y. Tan, R.J. Hamers, S. Jin, *Nano Lett.* 12 (2012) 724–731.
- [13] J. Zhang, Y. Ling, W. Gao, S. Wang, J. Li, *J. Mater. Chem. A* 1 (2013) 10677–10685.
- [14] F. Amano, M. Tian, G. Wu, B. Ohtani, A. Chen, *ACS Appl. Mater. Interf.* 3 (2011) 4047–4052.
- [15] Y. Qiu, S.-F. Leung, Q. Zhang, B. Hua, Q. Lin, Z. Wei, K.-H. Tsui, Y. Zhang, S. Yang, Z. Fan, *Nano Lett.* 14 (2014) 2123–2129.
- [16] V. Chakrapani, J. Thangala, M.K. Sunkara, *Int. J. Hydrogen Energy* 34 (2009) 9050–9059.
- [17] N.R. de Tacconi, C.R. Chenthamarakshan, K. Rajeshwar, T. Pauport, D. Lincot, *Electrochem. Commun.* 5 (2003) 220–224.
- [18] A. Tacca, L. Meda, G. Marra, A. Savoini, S. Caramori, V. Cristino, C.A. Bignozzi, V.G. Pedro, P.P. Bolx, S. Gimenez, J. Bisquert, *Chem. Phys. Chem.* 13 (2012) 3034–3055.
- [19] X. Zhang, D. Chandra, M. Kajita, H. Takahashi, L. Dong, A. Shoji, K. Saito, T. Yui, M. Yagi, *Int. J. Hydrogen Energy* 39 (2014) 20736–20743.
- [20] Z. Jiao, J. Wang, L. Ke, X.W. Sun, H.V. Demir, *ACS Appl. Mater. Interf.* 3 (2011) 229–236.
- [21] J. Zhu, W. Li, J. Li, Y. Li, H. Hu, Y. Yang, *Electrochem. Acta* 112 (2013) 191–198.
- [22] M. de Respinis, G. de Temmerman, I. Tanyeli, Ma.C.M. van de Sanden, R.P. Doerner, M.J. Baldwin, R. van de Krol, *ACS Appl. Mater. Interf.* 5 (2013) 7621–7625.
- [23] C.D. Dushkin, S. Saita, K. Yoshie, Y. Yamaguchi, *Adv. Colloid Interf. Sci.* 88 (2000) 37–78.
- [24] E. Redel, R. Thomann, C. Janiak, *Chem. Commun.* (2008) 1789–1791.
- [25] C. Vollmer, E. Redel, K. Abu-Shandi, R. Thomann, H. Manyar, C. Hardacre, C. Janiak, *Chem. Eur. J.* 16 (2010) 3849–3858.
- [26] C. Schöttle, P. Bockstaller, D. Gerthsen, C. Feldmann, *Chem. Commun.* 50 (2014) 4547–4550.
- [27] S. Emin, M. fanetti, F.A. Abdi, D. Lisjak, M. Valant, R. van de Krol, B. Dam, *ACS Appl. Mater. Interf.* 5 (2013) 1113–1121.
- [28] J.A. Moss, J.C. Yang, J.M. Stipkala, X. Wen, C.A. Bignozzi, G.J. Meyer, T.J. Meyer, *Inorg. Chem.* 43 (2004) 1784–1794.
- [29] N.F. Adegboyega, V.K. Sharma, K. Siskova, R. Zborzil, M. Sohn, B.J. Schultz, S. Banerjee, *Environ. Sci. Tech.* 47 (2013) 757–764.
- [30] S.R. Vishwakarma, J.P. Upadhyay, H.C. Prasad, *Thin Solid Films* 176 (1989) 99–110.
- [31] J. Booth, T. Ekström, E. Iguchi, R.J.D. Tilley, *J. Solid State Chem.* 41 (1982) 293–307.
- [32] B. Yang, L. Wang, J. Han, Y. Zhou, H. Song, S. Chen, J. Zhong, L. Lv, D. Niu, J. Tang, *Chem. Mater.* 26 (2014) 3135–3143.
- [33] J. Zhu, W. Li, J. Li, Y. Li, H. Hu, Y. Yang, *Electrochim. Acta* 112 (2013) 191–198.
- [34] X. Liu, F. Wang, Q. Wang, *Phys. Chem. Chem. Phys.* 14 (2012) 7894–7911.
- [35] K.-S. Ahn, S.-H. Lee, A.C. Dillon, C.E. Tracy, R. Pitts, *J. Appl. Phys.* 101 (2007) 093524.
- [36] Z.S. Houweling, J.W. Geus, M. de Jong, P.-P.R.M.L. Harks, K.H.M. van der Werf, R.E.I. Schropp, *Mater. Chem. Phys.* 131 (2011) 375–386.
- [37] C. Ng, A. Iwase, Y.H. Ng, R. Amal, *Chem. Sus. Chem.* 6 (2013) 291–298.
- [38] J.C. Hill, K.S. Choi, *J. Phys. Chem. C* 116 (2012) 7612–7620.
- [39] W.H. Lai, Y.H. Su, L.G. Teoh, Y.T. Tsai, M.H. Hon, *Mater. Trans.* 48 (2007) 1575–1577.
- [40] J.M. Spurgeon, J.M. Velazquez, M.T. McDowell, *Phys. Chem. Chem. Phys.* 16 (2014) 3623–3631.
- [41] A.J.E. Rettie, K.C. Klavetter, J.-F. Lin, A. Dolocan, H. Celio, A. Ishiekwe, H.L. Bolton, K.N. Pearson, N.T. Hahn, C.B. Mullins, *Chem. Mater.* 26 (2014) 1670–1677.
- [42] B. Cole, B. Marsen, E. Miller, Y. Yan, B. To, K. Jones, M. Al-Jassim, *J. Phys. Chem. C* 112 (2008) 5213–5220.
- [43] K.H. Ng, L.J. Minggu, M.B. Kassim, *Int. J. Hydrogen Energ.* 38 (2013) 9585–9591.